Microwave-assisted ionic liquid synthesis of Ti^{3+} self-doped TiO$_2$ hollow nanocrystals with enhanced visible-light photoactivity

Yu Chen, Weizun Li[*], Jingyu Wang, Yalan Gan, Le Liu, Meiting Ju[*]

College of Environmental Science and Engineering, Nankai University, Tianjin 300071, China

ARTICLE INFO

ABSTRACT

The realization of Ti^{3+} self-doping and exposure of a hollow structure in TiO$_2$ photocatalysts has been proven to be an effective approach for significantly improving their photocatalytic performance. Herein, a facile and green strategy that consists of microwave-assisted ionic liquid synthesis followed by a vacuum-activation process is developed for synthesizing highly active Ti^{3+} self-doping TiO$_2$ with a hollow structure. The results of X-ray diffraction, N$_2$ sorption, Raman, X-ray photoelectron spectroscopy, fluorescence spectrophotometry, scanning electron microscopy transmission electron microscopy and scanning transmission electron microscopy analyses revealed that the presence of the ionic liquid [Bmim][BF$_4$] acted not only as a microwave absorbent for the solvothermal process but also as a morphology-controlling agent via a dissolution-recrystallization process, leading to a mesoporous structure. Moreover, the subsequent vacuum calcination process modified the TiO$_2$ to provide highly air-stable Ti^{3+} and oxygen vacancies. Compared with the benchmark material P25 and other TiO$_2$ nanostructures synthesized using [Bmim]Cl and different molar ratios of [Bmim][BF$_4$], the Ti^{3+} self-doped TiO$_2$ with a hollow structure was used as an efficient photocatalyst, and it exhibited a 4.6-fold enhancement in photocatalytic activity for the selective oxidation of benzyl alcohol due to its enhanced visible-light absorption, efficient molecular oxygen adsorption ability and improved charge-separation efficiency under visible-light irradiation. Furthermore, the unique disordered core/ordered shell protects the TiO$_{2-x}$ nanoparticle core from further oxidation and effectively blocks oxidation between the Ti^{3+} and dissolved oxygen in the solvent, thereby allowing long-term recycling stability. The possible reaction mechanism for the photocatalytic selective oxidation of benzyl alcohol over Ti^{3+} self-doped TiO$_2$ hollow nanocrystals has also been investigated. The results obtained in this study may shed light on improving the photoactivity in fabricating defective TiO$_2$ and defect-based nanostructures and their applications in solar energy conversion.

© 2016 Elsevier B.V. All rights reserved.

1. Introduction

Titanium dioxide (TiO$_2$), a widely investigated semiconductor, can be utilized in environmental and energy applications, particularly in photocatalysis, due to its good photocatalytic activity, high chemical and thermal stabilities, nontoxicity, and excellent degradation capacity [1–7]. However, the practical application of TiO$_2$ has been impeded by its low efficiency for utilizing solar energy and its low quantum yield resulting from its wide band gap and high recombination rate of photogenerated charge carriers [8]. Several strategies have been proposed to overcome these issues. Doping with metal or non-metal elements is known to be a feasible approach for tuning the electronic structure of TiO$_2$ and for introducing new states into the TiO$_2$ band gap for visible light [2,9–13]. In general, doping with non-metal elements, such as C, N and S, can build acceptor states above the valence band from the p states of non-metal ions, and doping with metal elements, such as Fe and Cr, can create donor states below the conduction band. However, for doped TiO$_2$, the lattice defects induced by the dopants will unavoidably introduce new charge-carrier traps and recombination centers, which consequently might exert a negative effect on the photocatalytic activity.

Compared with the conventional doping methods, Ti^{3+} doped TiO$_2$ has been demonstrated to exhibit enhanced visible-light absorption, which is attributed to the introduction of an electronic state band below the conduction band minimum of TiO$_2$ through an oxygen vacancy or Ti^{3+} doping [14–18]. Furthermore,

theoretical studies have suggested that the concentration of Ti^{3+} plays a decisive role in producing a facile transfer of an electron or hole to obtain efficient activity in the visible spectrum [19,20]. Recently, chemistry of structurally defective TiO_2 with Ti^{3+} doping (or oxygen vacancies) has been developed to address the above challenges [21–28]. In general, reduction can be achieved using harsh and expensive physical methods, such as high-temperature and high-pressure hydrogenation, plasma treatment and electron beam irradiation. Considering all of these disadvantages associated with the reduction-based synthesis of Ti^{3+}-doped TiO_2, the counter-intuitive strategy, that is, using a low-temperature vacuum-activated method to modify the TiO_2, becomes an appealing choice [29].

In addition, hollow structures have recently attracted a considerable amount of attention [30–33]. As a unique structure, hollow TiO_2 can exhibit substantially improved photocatalytic activity as a result of the synergistic effects of the shortened bulk diffusion length of carriers with the decreased bulk recombination and increased reactive sites. For instance, Jiao et al. [34] synthesized hollow anatase TiO_2 single-crystalline nanocrystals and mesocrystals with dominant {101} facets through a route using PO_4^{3-}/F^- as the morphology-controlling agent, and they found that compared to solid single crystals, the hollow and mesocrystals can exhibit substantially improved photocatalytic activity (O_2/H_2 evolution from water splitting and CH_4 generation from photoreduction of CO_2). Ren et al. [35] demonstrated the preparation of TiO_2 nanocrystals with internal pores through a facile microwave-assisted hydrolysis of a $TiOCl_2$ aqueous solution in the presence of HF followed by calcination. The as-prepared TiO_2 nanocrystals with internal pores exhibited considerably higher photocatalytic activity than solid nanocrystals for the photodegradation of crystal violet, methyl orange, and 4-chlorophenol. Previous reports suggested that the presence of F species is crucial in the formation of TiO_2 nanocrystals with hollow structures. Moreover, increasing attention has been focused on developing TiO_2 with a hollow structure through a simple hydrothermal synthesis in the presence of HF or ammonium fluoride (NH_4F) as the shape-controlling agent. However, the construction of visible-light responsive hollow-structure TiO_2 nanocrystals self-doped with Ti^{3+} has not been realized.

Herein, we successfully developed an effective strategy for the synthesis of Ti^{3+} self-doped TiO_2 nanocrystals with a hollow structure using a microwave-assisted ionic liquid solvothermal approach followed by a vacuum-activation method. The choice of the ionic liquid [Bmim][BF_4] used here served not only as the microwave absorbent but also as a green solvent providing F anions. Furthermore, the influence of the amount of ionic liquid on the physicochemical properties and photocatalytic activity of the resulting TiO_2 nanocrystals was studied. Then, the photocatalytic activity of the obtained Ti^{3+}-doped hollow TiO_2 nanocrystals in the decoloration of methylene blue and the oxidation of benzyl alcohol under visible-light irradiation was investigated. The photocatalytic mechanism for the selective oxidation of benzyl alcohol over Ti^{3+} self-doped TiO_2 is also proposed. The as-prepared TiO_{2-x} photocatalyst contained high contents of Ti^{3+}-dopants and possessed a hollow structure. The Ti^{3+}- dopants in the TiO_2 lattice could provide the electronic charge required for O_2 adsorption and dissociation and narrow the energy band gap of the TiO_2 semiconductor via the formation of intermediate energy levels, and the hollow structure shortened the bulk diffusion length of charge carriers and increased the number of reactive sites, leading to a vastly superior visible photocatalyst. Furthermore, the unique ordered shell protects the disordered core from further oxidation and effectively blocks oxidation between the Ti^{3+} and dissolved oxygen in the solvent, thereby allowing long-term recycling stability.

2. Experimental

2.1. Materials

The ionic liquids 1-butyl-3-methylimidazolium tetrafluoroborate ([Bmim][BF_4]) and 1-n-butyl-3-methylimidazolium chloride ([Bmim]Cl) were obtained from Lanzhou Institute of Chemical Physics, China. Tetra-butyl titanate (TBT) was purchased from Alfa Aesar Chemical Co. All chemicals were of analytical grade and were used as received without any further purification.

2.2. Preparation of catalysts

Anatase TiO_2 nanocrystals were synthesized in a quaternary solution system consisting of TBT, deionized water, [Bmim][BF_4]([Bmim]Cl) and acetic acid (HAc), with molar ratios of TBT/H_2O/[Bmim][BF_4]/HAc according to Table 1. In a typical synthesis, 3.54 mL of HAc, 0.35 mL of water, and 4.372 mL of [Bmim][BF_4] were mixed in a Teflon beaker. Then, TBT was added to the solution under magnetic stirring, and the solution became transparent. Finally, the homogeneous solution was transferred to a 70 mL Teflon-lined autoclave, which was then placed in a microwave-solvothermal synthesis system (MDS-6, Sineo, Shanghai, China) and maintained at 150 °C for 1 h. After cooling to room temperature, the resulting powder was separated by centrifugation, washed several times with ethanol and deionized water, dried at 60 °C for 12 h, and finally calcined at 200 °C for 6 h in a vacuum oven. The vacuum-activated TiO_2 was labeled as $TiO_{2-Fvacuum}$, and the as-prepared TiO_2 were labeled as TiO_{2-F} and TiO_{2-Cl}. To investigate the effect of the ionic liquid [Bmim][BF_4] on photocatalytic activity, a series of Ti^{3+} self-doped TiO_{2-x} (with different molar ratios of [Bmim][BF_4]-Ti, Rf = 0, 0.1, 0.2, 0.5, 1, 2, and 5) nanoparticles were synthesized using different feed ratios by varying the amount of [Bmim][BF_4], followed by calcining in a vacuum oven at 200 °C for 6 h; these samples were denoted as S1–S7, respectively.

2.3. Sample characterization

To identify the TiO_2 phases, X-ray diffraction (XRD) measurements were performed using a PANalytical X'pert MRD with a step size of 0.02° in the region of 2θ = 10–80°. Diffuse reflectance UV–vis spectra of the samples (ca. 20 mg diluted in ca. 80 mg of $BaSO_4$) were recorded in air against $BaSO_4$ in the region of 200–800 nm on a Shimadzu 3600 UV–vis spectrophotometer. The morphologies of the TiO_2 composites were measured by scanning electron microscopy (SEM) on a Hitachi S-4800 microscope. Transmission electron microscopy (TEM) images and high-resolution TEM (HRTEM) images were recorded using an FEI Tecnai G2-F20 microscope at an accelerating voltage of 200 kV. Energy-dispersive X-ray (EDX) and EDX elemental mapping were performed on Oxford-Instruments X-MaxN to visualize the elemental compositions of the products. X-ray photoelectron spectra (XPS) of the samples

Table 1
The molar ratios of starting materials in the TBT/H_2O/[Bmim][BF_4] ([Bmim]Cl)/HAc system with various molar ratios of 1:x:y:z.

Sample	TBT	H_2O	HAc	[Bmim][BF_4]	[Bmim]Cl
TiO_{2-F}	1	1.66	5	2	0
TiO_{2-Cl}	1	1.66	5	0	2
S1	1	1.66	5	0	0
S2	1	1.66	5	0.1	0
S3	1	1.66	5	0.2	0
S4	1	1.66	5	0.5	0
S5	1	1.66	5	1	0
S6	1	1.66	5	2	0
S7	1	1.66	5	5	0

were recorded on a Thermo Fisher Scientific ESCALAB 250XI using a monochromated Al-Ka X-ray source. Accurate binding energies (± 0.1 eV) were determined with respect to the position of the adventitious C 1s peak at 284.6 eV. Raman analysis was performed using a Renishaw InVia Raman spectrometer, and spectra were obtained with the green line of an Ar-ion laser (514.53 nm) in a micro-Raman configuration. Photoluminescence (PL) spectra were measured at room temperature using a fluorescence spectrophotometer (F-7000, Hitachi, Japan). The excitation wavelength was 300 nm, and the scanning speed was 1200 nm/min. The specific surface areas were determined through N_2 adsorption/desorption isotherms collected at $-196\,°C$ on a TriStar II 3020 adsorption analyzer. The samples were degassed under vacuum at $200\,°C$ for 4 h prior to analysis. Thermogravimetric analysis (TGA) was conducted using a NETZSCH TG209 thermogravimetric analyzer with a heating rate of $10\,°C\,min^{-1}$ under an N_2 atmosphere. Electron spin resonance (ESR) spectra were recorded at 100 K using a Bruker ER200-SRC.

2.4. Photocatalytic activity measurement

The photocatalytic activity of TiO_2 was estimated from the degradation of methylene blue (MB). In a 100 mL MB aqueous solution (20 mg/L), 0.2 g of catalyst was dispersed in a beaker, and the distance between the solution and the lamp was fixed at 10 cm (the excitation power density was $80\,mW\,cm^{-2}$). The suspension was stirred in the dark for 30 min until the concentration of MB no longer changed, indicating the adsorption equilibrium of MB. As an irradiation source, a 300 W xenon lamp (PLS-SXE300, Beijing Trusttech Co., Ltd.) with a 400 nm cut-off filter was used in the experiment. The absorbance of the solution was recorded on a UV–vis absorption photometer (UV-3100, MAPADA Analytic Apparatus Ltd. Inc., Shanghai, China) at a wavelength of 664 nm. Benzyl alcohol oxidation was performed in a home-made reactor equipped with a borosilicate glass window for illumination. Typically, 20 mg of TiO_2 was spread into the reactor, and then 20 mL of toluene (solvent), 0.1 mmol of benzyl alcohol (reactant), and 50 μL of undecane (internal standard) were injected into the reactor. O_2 was bubbled through the mixture at a rate of $20\,mL\,min^{-1}$. The reactor was photoirradiated under magnetic stirring using a 300 W xenon lamp filtered through a glass filter to provide light with wavelengths $\lambda > 400$ nm with an irradiation intensity of $80\,mW\,cm^{-2}$. Cooling water was used to eliminate the thermal effect in the reaction. The products were analyzed using a gas chromatograph system (TRACE 1310GC, Thermo Fisher) with a flame ionization detector (FID). After the photocatalytic reaction, the catalysts were carefully washed with anhydrous ethanol and deionized water. Finally, the catalysts were dried in a vacuum oven at $80\,°C$ overnight for the following cycling photoactivity test. Control photoactivity experiments using different radical scavengers (ethylenediaminetetraacetic acid disodium salt (EDTA-2Na) as a scavenger for photogenerated holes, *tert*-butyl alcohol as a scavenger for hydroxyl radicals, $AgNO_3$ as a scavenger for electrons, and benzoquinone as a scavenger for superoxide radical species) were performed similar to the above photocatalytic oxidation of alcohols except that radical scavengers (0.1 mmol) were added to the reaction system. The conversion of benzyl alcohol and yield of benzaldehyde were defined as follows:

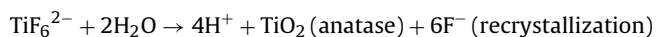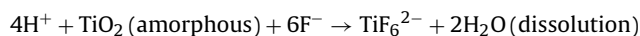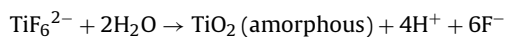$$\text{Conversion} (\%) = \left[(C_0 - C_{\text{alcohol}}) / C_0 \right] \times 100$$

$$\text{Yield} (\%) = C_{\text{aldehyde}} / C_0 \times 100$$

$$\text{Selectivity} (\%) = \left[C_{\text{aldehyde}} / (C_0 - C_{\text{alcohol}}) \right] \times 100$$

where C_0 is the total amount of alcohols in the solution prior to illumination; C_{alcohol} is the amount of alcohols in the solution after illumination for 7 h; and C_{aldehyde} is the amount of aldehyde in the solution after illumination for 7 h.

3. Results and discussion

The TGA results (Fig. S1) confirm the thermal stability of the as-prepared samples, which can retain their states up to $600\,°C$ without obvious weight loss, indicating the absence of organic species. It has been reported that the ionic liquid [Bmim][BF_4] can be used as a morphology-directing agent for synthesizing TiO_2 crystals with various morphologies [36–39]. In this case, the morphologies of TiO_2 samples prepared using an ionic liquid were characterized using FE-SEM and TEM. As shown in the SEM and TEM images (Fig. 1a and c), the obtained calcined TiO_2 nanocrystals are uniform, and the majority of these nanocrystals adopt cube-like or truncated octahedral bipyramidal shapes with an average diameter of $\sim$20 nm. The HRTEM image (Fig. 2d) shows that the TiO_2 nanocrystals are well crystallized, and the d-spacings of 0.23 nm and 0.35 nm corresponding to the (001) and (101) crystal lattices of anatase TiO_2 are clearly observed. This result is in accordance with recent syntheses performed under aqueous conditions, in which the use of fluorine-containing species results in the preferential exposure of the {001} facet of anatase, thereby truncating the bipyramidal base morphology of the nanocrystals [40]. For comparison, Fig. S2 (a and b) presents the result obtained by replacing [Bmim][BF_4] with [Bmim]Cl under otherwise identical conditions. When [Bmim]Cl was added, only nanorods of anatase particles were produced. HRTEM analysis confirms that {100} facets are the dominant facets in this sample, as well as {101} facets and {001} facets (Fig. S2). Furthermore, note that there are several wormhole-like mesopores present in each of the TiO_2 particles (Fig. 1(c) and (d)), and the hollow structure is clearly visible with a dark-field image, as shown in Fig. 2b. To further illustrate the hollow structure, high-angle annular dark field (HAADF) imaging coupled with a spatially resolved energy-dispersive X-ray spectrometer (EDS) was performed using scanning transmission electron microscopy (STEM). Fig. 2 shows a typical annular dark-field TEM image taken from a TiO_2 nanocrystal, along with corresponding Ti, O, and F maps. As visually traced from the high-resolution HAADF image, the TiO_2 nanocrystals contain two sizes of mesopores: the dominate mesopores are approximately 2–3 nm, and the others are 6–7 nm. This result is consistent with the statistical cavity size (inset of Fig. 1c) of the TEM image. The element mapping images of Ti, O, and F exhibit a harmonious ravine distribution throughout the hollow nanocrystal, further verifying the hollow nature of the as-prepared TiO_2 nanocrystals. It has previously been reported that the presence of fluoride ions in a lower concentration favors the exposure of {001} facets through preferential adsorption and that a higher concentration would selectively induce preferential dissolution of the amorphous particle interior and concurrent deposition of a porous crystalline external shell to produce an intact hollow structure according to the following equations [41–43]:

$$TiF_6{}^{2-} + 2H_2O \rightarrow TiO_2\,(\text{amorphous}) + 4H^+ + 6F^-$$

$$4H^+ + TiO_2\,(\text{amorphous}) + 6F^- \rightarrow TiF_6{}^{2-} + 2H_2O\,(\text{dissolution})$$

$$TiF_6{}^{2-} + 2H_2O \rightarrow 4H^+ + TiO_2\,(\text{anatase}) + 6F^-\,(\text{recrystallization})$$

Therefore, it is strongly believed that the ionic liquid [Bmim][BF_4] adsorbed on facets of anatase nanocrystals, which played key roles in controlling the crystallization process via controlling the aggregation behavior of the nanocrystals. Moreover, as revealed by the HAADF-STEM image and element mapping images (Fig. S3), the
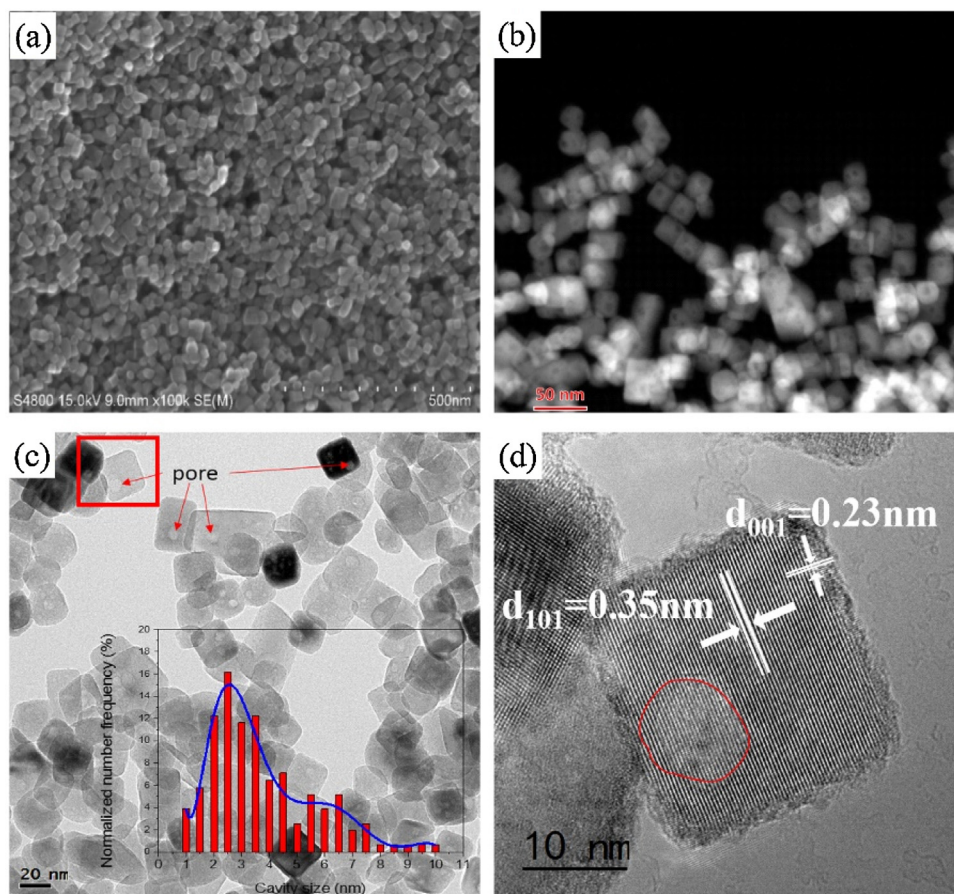
Fig. 1. SEM image (a), HAADF-STEM image (b), and TEM image (c) of Ti^{3+} self-doped TiO_2 with a hollow structure. The inset is the pore size distribution of the TiO_2 nanocrystals with a mesoporous structure. The arrows indicate some typical pores of the hollow structure. HRTEM image (d) of Ti^{3+} self-doped TiO_2 with a hollow structure.
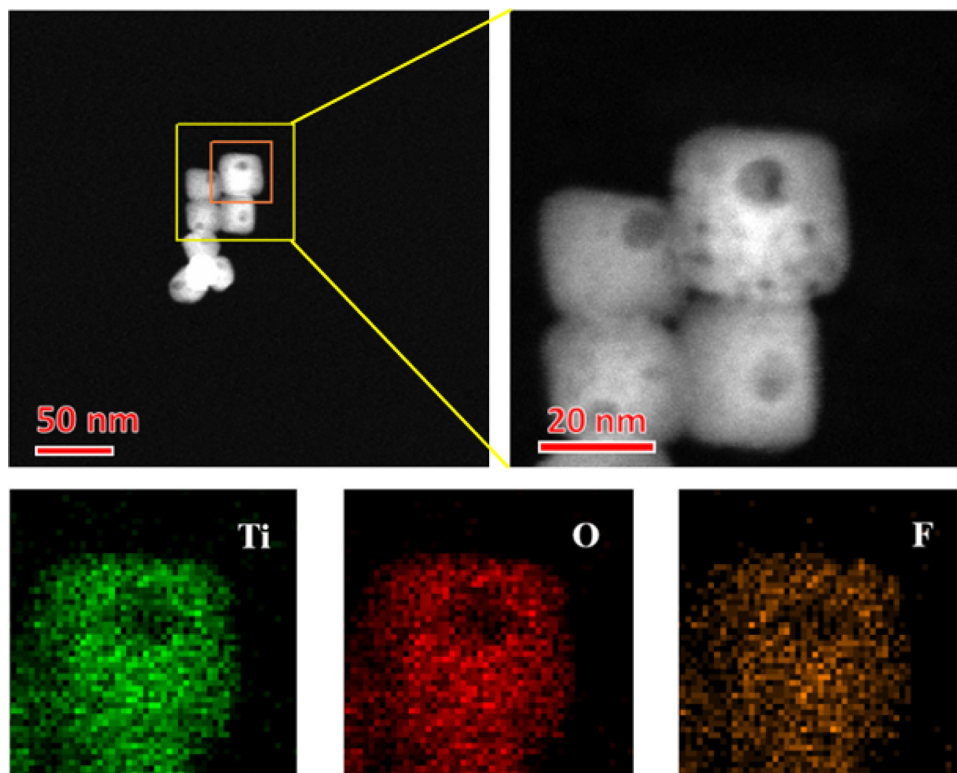

Fig. 2. HAADF–STEM images and STEM-EDS elemental mapping of Ti^{3+} self-doped TiO_2 with a hollow structure.
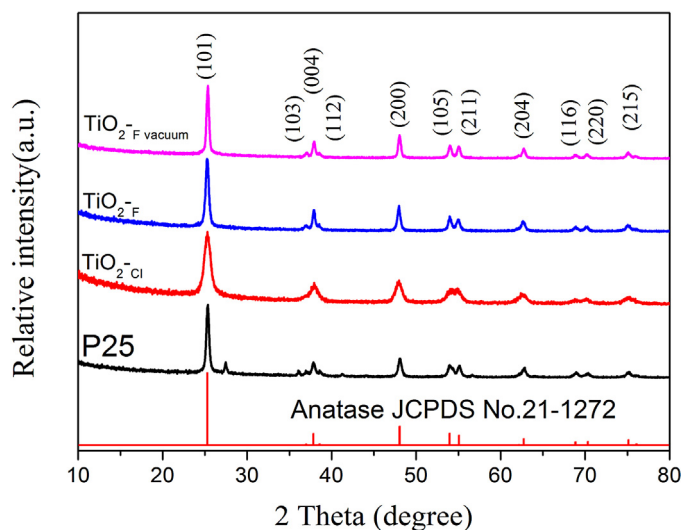
Fig. 3. X-ray diffraction patterns of TiO_2 obtained from [Bmim]Cl and [Bmim][BF$_4$] with and without vacuum treatment.

Fig. 4. N$_2$ adsorption-desorption isotherm and BJH desorption pore size distribution (inset) of the TiO_2 nanocrystals prepared from [Bmim][BF$_4$] with and without vacuum treatment.

wormhole-like mesopores still remained in the TiO_2 nanocrystals after five photoreaction cycles. This result indicated that the hollow structure maintained for a long cycling stability.

The crystal structures of the TiO_2 nanocrystals were investigated through the XRD patterns. As shown in Figs. 3 and S4, all of the as-received TiO_2 samples were well crystallized by the microwave-assisted ionic liquid solvothermal treatment. It is well known that microwave irradiation leads to the formation of numerous "hot spots" during the local superheating of the aqueous solution, which leads to nucleation and crystal growth and massive seeds throughout the bulk solution [44,45]. In our current system, to compare the effect of microwave irradiation with conventional heating methods, we used the hydrothermal route rather than microwave heating to perform controlled experiments to prepare representative TiO_2 nanocrystals under similar synthetic conditions. It was found that TiO_2 nanocrystals can be obtained by hydrothermal heating at 150 °C for a relatively long period of time (24 h). The shapes (Fig. S2 (c and d)) of the resulting TiO_2 nanocrystals are a mixture of cube-like and truncated octahedral bipyramids with an average diameter of ∼36 nm. Therefore, the rate of crystal growth is significantly accelerated relative to that under the conventional heating method, and the shorter microwave heating time leads to enhanced efficiency and significant energy savings. This particularity can be attributed to the different of heating mechanism of these two heating modes [45]. Conventional heating in hydrothermal processes relies on thermal conduction of black-body radiation to drive chemical reactions, in which the reaction vessel serves as an intermediary for transferring energy from the heating source to the solvent and finally to the reactant molecules. In contrast, the particularity of microwave heating is the volumetric nature of the power dissipation in a dielectric, which directly couples microwave energy to the molecules that are present in the reaction mixture. Furthermore, TiO_2 nanocrystals synthesized with the ionic liquids [Bmim][BF$_4$] and [Bmim]Cl have a typical anatase structure without any impurity phases, in agreement with JCPDS card No. 21-1272. The characteristic diffraction peaks located at 25°, 38°, 48°, 54°, 55°, 63°, 69°, 70°, and 75° can be well indexed to the lattice planes of (101), (004), (200), (105), (211), (204), (116), (220), and (205) of anatase phase TiO_2 nanostructures. Based on the linewidth analysis of the anatase (101) diffraction peak, the average crystal sizes of all of these samples estimated using the Scherer equation are summarized in Table 2. As shown in Table 2, changing of the raw ionic liquid to [Bmim]Cl significantly affected the grain size of the TiO_2
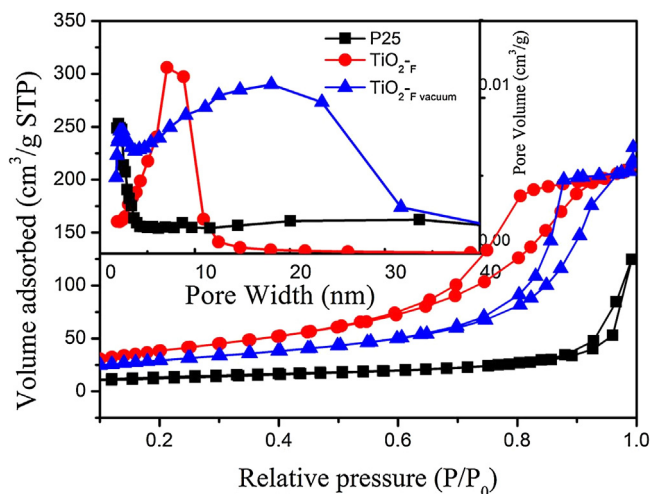
nanoparticles. Further examination of Fig. S4 shows that the intensity of the anatase XRD peaks steadily increases and that the width becomes slightly narrower with the addition of the ionic liquid [Bmim][BF$_4$], indicating that the crystal sizes of the TiO_2 increased steadily and that the crystallization was enhanced. This result is consistent with a previous report that the fluorine species can enhance the crystallization of the anatase phase [46]. Here, the ionic liquid [Bmim][BF$_4$] is a type of good microwave absorbent due to its ionic nature, and its boiling temperature is thus reached within a very short time under microwave irradiation. Then, it immediately dissociates into F$^-$ ions in the presence of water molecules according to the following reaction:

$$[BF_4]^- + H_2O \rightarrow BF_3 \cdot H_2O + F^-$$
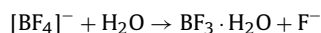
Consequently, a F ion-rich environment is thus established, similar to the case in which HF is used as the fluorinating agent. This result indicated that the ionic liquid [Bmim][BF$_4$], in the present experiment, acted not only as a microwave absorbent for the solvothermal process but also as a promotive agent for the growth of the nanoparticles.

To determine the surface area and pore-size distribution of the obtained TiO_2 hollow nanocrystals, BET characterization was conducted. Fig. 4 presents the nitrogen adsorption-desorption isotherms and the corresponding pore-size distributions of commercial benchmark materials of P25 and the as-prepared and vacuum-activated TiO_2 hollow nanocrystals obtained using [Bmim][BF$_4$]. It can be observed that all three samples exhibited a type IV nitrogen isotherm with a H2 hysteresis loop. Compared with the commercial P25, both TiO_{2-F} and $TiO_{2-Fvacuum}$ presented a hysteresis loop with a higher relative pressure range, thus providing evidence that the TiO_2 obtained using [Bmim][BF$_4$] possesses mesoporous characteristics with assembly behavior. Furthermore, the hysteresis loop for vacuum-activated TiO_2 hollow nanocrystals appeared in a higher relative pressure range of 0.7–1.0 compared to the as-prepared TiO_2, suggesting the existence of large mesopores. These results suggest that the calcination at 200 °C leads to the coalition of small pores into large-size pores accompanying the TiO_2 nanocrystal growth. The plot of the pore size distribution was determined by using the BJH method from the desorption branch of the isotherm. The pore size distribution of $TiO_{2-Fvacuum}$ is in a quite wide range of 0–40 nm, which is consistent with the pore size suggested by the TEM results (Fig. 1c inset). The porous structures of TiO_2 are considered to be extremely useful in photocatalysis

Table 2
Physical-chemical properties of TiO$_2$ samples.

Sample	Phase[a]	Crystalline size[b](nm)	S$_{BET}$ (m^2/g)	Pore size (nm)	Pore volume (cm^3/g)
P25	A+R	24.9(A)	43.08	17.91	0.19
TiO$_{2-F}$	A	19.8	97.53	12.17	0.26
TiO$_{2-F}$ vacuum	A	20.3	94.13	11.68	0.23
TiO$_{2-Cl}$	A	13.5	129.12	8.81	0.33
S1	A	7.9	242.27	5.21	0.57
S2	A	10.8	125.25	7.16	0.35
S3	A	10.2	118.82	9.92	0.29
S4	A	15.2	112.29	10.35	0.30
S5	A	17.4	101.87	12.17	0.25
S6	A	20.3	94.13	11.68	0.23
S7	A	23.8	58.29	10.88	0.18

[a] A and R denote anatase and rutile, respectively.
[b] Crystal size of TiO$_2$ calculated according to the Scherrer equation.

[47,48]. They may shorten the bulk diffusion length of charge carriers and provide flexible transport pathways for the diffusion of reactants during the photocatalytic process. Table 2 summarizes the effect of the amount of the ionic liquid on the S$_{BET}$, pore size, and pore volume of the samples. The S$_{BET}$ values of these prepared samples were all greater than 90 m^2/g, which are almost two-fold greater than that of P25. Moreover, the specific surface area greatly decreased when the amount of [Bmim][BF$_4$] increased from 0 to 5. This result can be attributed to the growth of TiO$_2$ nanocrystals induced by the introduction of the ionic liquid [Bmim][BF$_4$], as confirmed by the aforementioned XRD results.

The model for the formation of the anatase NCs is described in Scheme 1, in which the entire process is divided into four stages. In this study, TBT and ionic liquid are selected as the titanium precursor and solvent, respectively. TBT is widely used for the synthesis of titania and is very reactive to water, forming titanium hydroxide. Note that the reaction is very slow at room temperature, and reaction temperatures of 80–150 °C are generally required to obtain reasonable rates and crystalline products. The classical LaMer model can be introduced here to address the nucleation and growth kinetics of nanoparticles [49]. The process of nanocrystal formation is classically divided into two events: nucleation and growth. For microwave-assisted ionic liquid synthesis, the mixture is heated to the reaction temperature (150 °C) in a very short time (2 min), which leads to the formation of a large amount of crystal nuclei. Once the nucleation begins, the reaction system immediately enters the growth process, and the nuclei grow rapidly. In this case, the overall processes containing nucleation and growth are drastically shorted by the rapid heating of the microwave method. The microwave nucleated precursors had a higher population of nuclei with smaller sizes than the precursors nucleated by conventional heating [50]. During the transient stage of nucleation, many small crystals easily contact each other to be assembled and ripened into the final nanocrystals. In this stage, different aggregation behaviors occurred in F$^-$- and Cl$^-$-mediated processes due to the natures of small crystals. It was hypothesized that [Bmim]$^+$ should interact with the bulk through hydrogen bonds or electrostatic force, which would induce the oriented arrangement of the BF$_4^-$ and Cl$^-$ anions along the wall and pile up and stack, possibly by π-π interactions or other noncovalent interactions between the imidazole rings [51]. For F-complexed anatase small crystals, {101} facets possessed higher surface energy, and they tended to aggregate toward {101} facets to eliminate high-energy facets. In contrast, the Cl- complexed anatase small crystal {001} facets possessed higher surface energy, and they tended to aggregate along the [001] directions. Therefore, cube-like and elongated rod-like TiO$_2$ nanocrystals were formed via these two different routes, respectively. During the ripening process, hollow nanocrystals formed due to fluoride-mediated self-transformation of amorphous titania solid nanocrystals, in which fluoride induces
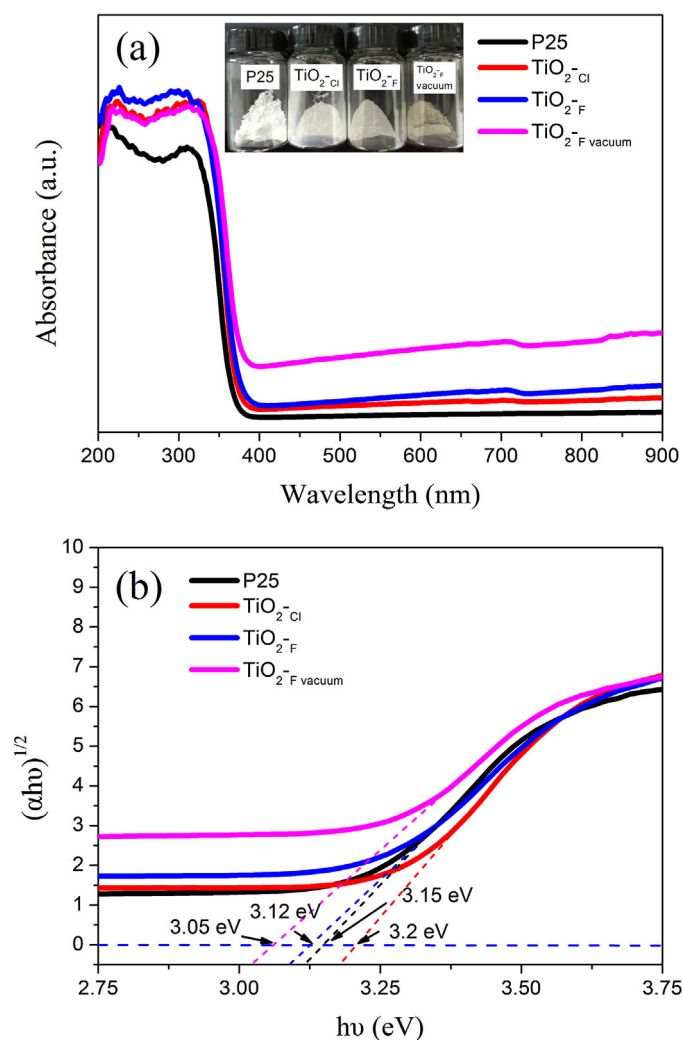

Fig. 5. (a) UV–vis diffuse reflectance spectra of Degussa P25 and the TiO$_2$ obtained from [Bmim]Cl and [Bmim][BF$_4$] with and without vacuum treatment. The top insert is a digital photograph of the four samples. (b) Curves of Kubelka-Munk function as the vertical axis and plotted against the photon energy.

both the dissolution of the particle interior and subsequent mass transfer from the core to the external surface [52,53].

The optical response of the vacuum-activated TiO$_2$ hollow nanocrystals prepared from [Bmim][BF$_4$] compared to that of commercial Degussa P25 and untreated TiO$_2$-$_F$ and TiO$_2$-$_{Cl}$ is shown in Fig. 5. It can be observed that all of the samples only responded to ultraviolet light due to their intrinsic wide band gap.
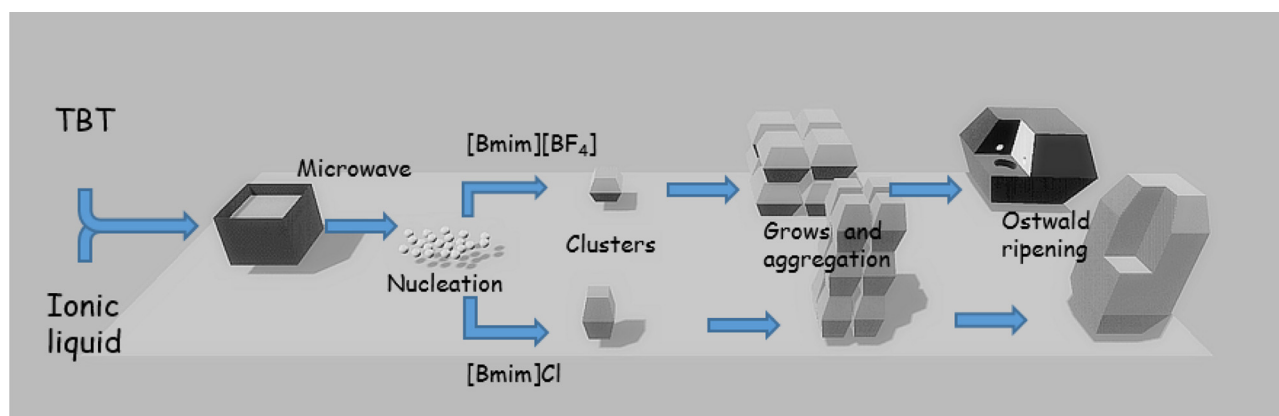
Scheme 1. Schematic illustration of the two different morphologies of anatase TiO_2 nanocrystals, formation and shape evolution.

For the vacuum-activated TiO_2, a strong broad absorption band between 400 and 800 nm, covering nearly the entire visible range, is observed, which is consistent with the change in color of the powders from white to brown (inset in Fig. 5a). Brown coloration has previously been reported in reduced TiO_{2-x} and is characteristic of free electrons in TiO_2 conduction band, and the additional electrons are proposed to result from oxygen vacancies or Ti^{3+}, which are formed during the vacuum-activation process [54]. Because titania is an indirect semiconductor, plots of $(ahv)^{1/2}$ versus the energy of the absorbed light will provide the band gap of the titania samples. Fig. 5b shows that the calculated band gap energies are 3.05 eV and 3.2 eV for Ti^{3+} self-doped TiO_2 ($TiO_{2-Fvacuum}$) and undoped TiO_2 (TiO_{2-Cl}), respectively. It is clear that the formation of Ti^{3+} centers will have an influence on the optoelectronic behavior of photocatalytic materials. In this sense, the origin of the lower energy of the band gap is likely to be related to the presence, localization, and amount of these Ti^{3+} centers. As it has been demonstrated, the energy levels corresponding to the Ti^{3+}-reduced states are extremely shallow; the excess electrons tend to be delocalized over several of these Ti centers, and consequently, the Fermi level lies at the boundary or even in the lower region of the conduction band. When the concentration of Ti^{3+} states is greatly increased, a type of sub-band is formed close to the bottom of the conduction band, eventually resulting in a small but clear red shift of the optical band gap (almost 0.15 eV from that of pristine anatase TiO_2).

To further examine the structural characteristics and crystal defects of Ti^{3+} self-doped TiO_2 hollow nanocrystals, Raman spectral measurements were conducted (Fig. 6). Degussa P25 and TiO_2 obtained from [Bmim]Cl with the same phase composition were employed in the analysis as reference samples. The anatase structure is characterized by the tetragonal space group I41/amd, and six Raman transitions ($1A_{1g}$, $2B_{1g}$, and $3E_g$) are allowed according to the factor group analysis [55]. In the present study, four Raman active modes of E_g (140 cm^{-1}), B_{1g} (395 cm^{-1}), A_{1g} (515 cm^{-1}) and E_g (635 cm^{-1}) are observed. This result clearly indicates that the well-crystallized anatase structure is preserved in the microwave-assisted solvothermal synthesis. More importantly, the most remarkable feature is that the predominate peak position undergoes a blue shift from 144.6 cm^{-1} to 151.3 cm^{-1} accompanied by peak broadening for the Ti^{3+} self-doped TiO_2 sample compared to P25. As previously reported [56,57], the E_g mode shift and broadened linewidth of TiO_2 in the Raman spectrum can be attributed to lattice disorder or localized defects associated with Ti^{3+} or oxygen vacancies. Thus, the blue shift of E_g mode for 6.7 cm^{-1} found in TiO_{2-x} samples and the broadening of the peaks support the presence of lattice disorder (nonstoichiometric) and crystal domain size effect.
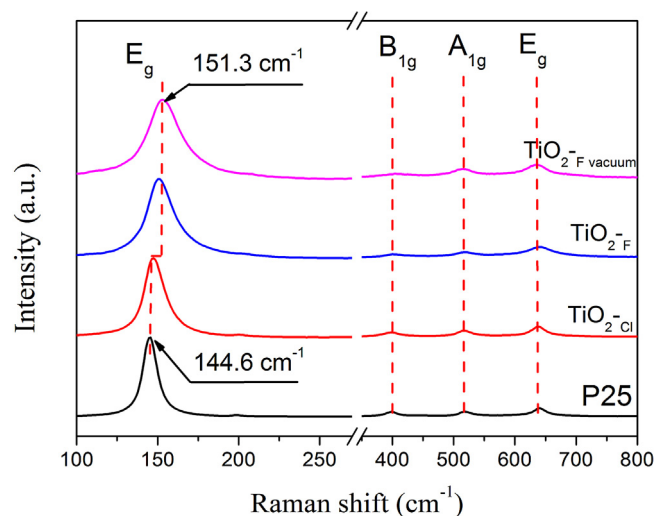
Fig. 6. Raman spectra of Degussa P25 and the TiO_2 obtained from [Bmim]Cl and [Bmim][BF$_4$] with and without vacuum treatment.

We also measured the photoluminescence (PL) emission of the samples to understand the behavior of light-generated electrons and holes in our samples because PL emission is a result of the recombination of the free carriers. The PL spectra of Degussa P25, $TiO_{2-Fvacuum}$, TiO_{2-F} and TiO_{2-Cl} samples in the wavelength range of 350–700 nm with the excitation light at 320 nm are shown in Fig. 7. The shapes of the emission spectra of the different samples are similar. Three main emission peaks are observed at 400 nm (3.10 eV), 423 nm (2.94 eV), and 441 nm (2.81 eV). A strong peak at approximately 400 nm is attributed to the emission of the band gap transition with the energy of light approximately equal to the bandgap energy of anatase (387.5 nm) [58]. In addition, there are four peaks observed in the wavelength range from 440 to 550 nm. These PL signals are due to excitonic PL, which primarily results from surface oxygen vacancies and defects of the TiO_2 samples. The PL peaks at 451 and 468 nm are attributed to band edge free excitons, and the other two peaks at 483 and 493 nm are attributed to bound excitons. The PL peak intensities of the $TiO_{2-Fvacuum}$ and TiO_{2-F} samples are considerably lower than those of Degussa P25 and TiO_{2-Cl}, and the vacuum-activated sample has the lowest intensity. This observation indicates that the TiO_2 with a hollow structure has a relatively low recombination rate of electrons and holes, which normally favors high photocatalytic activity [28].

To identify the effects of the surface elemental compositions of TiO_2 photocatalysts with various morphologies on their photocatalytic properties, XPS characterization of Ti, O, and F elements
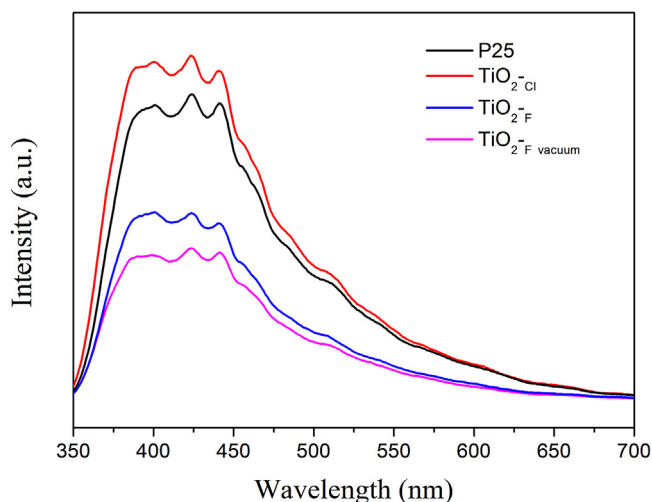
Fig. 7. Photoluminescence (PL) spectra of the Degussa P25, TiO$_{2\text{-Cl}}$, and TiO$_{2\text{-F}}$ with and without vacuum activation.

and survey scans of Degussa P25, TiO$_{2\text{-Fvacuum}}$, TiO$_{2\text{-F}}$, and TiO$_{2\text{-Cl}}$ were performed, which are shown in Figs. 8 and S5. The XPS results clearly indicated that Ti and O elements all appear in all catalysts, but the F element exists only in TiO$_2$ obtained from [Bmim][BF$_4$]. The center of the F1s (Fig. 8(b)) peak at 684.1 eV, which can be assigned to the typical value of F$^-$ in fluorine TiO$_2$ systems such as Ti-F species, can be clearly observed, suggesting that the fluorine bound to the surface of TiO$_2$ and does not indicate the presence of TiO$_{2-x}$F$_x$ species [59,60]. The XP spectra of Ti 2p were recorded to investigate the chemical state of Ti to obtain further insights into the Ti^{3+}-doped hollow nanocrystals. As shown in Fig. 8(a), for all samples, the Ti 2p$_{3/2}$ peak maximum is centered at 458.6 eV, and the peaks were highly symmetric, indicating absolute coordination of Ti^{4+} [61]. The peak at 464.3 eV is assigned to the 2p$_{1/2}$ core level of Ti^{4+} in TiO$_2$. From the XPS results, we clearly see that there is no detectable Ti at a lower oxidation state in the surface region of all samples, as indicated by the absence of the shoulder peaks associated with Ti^{3+} at 456.8 eV and 462.5 eV for the 2p3/2 and 2p1/2 core level of Ti^{3+}, respectively. Surprisingly, the Ti core-levels XP spectrum of the vacuum-activated sample is almost completely comparable to that of the Degussa P25 and TiO$_{2\text{-Cl}}$ samples, suggesting the existence of identical surface states of Ti in these samples. It is widely believed that Ti^{3+} is easily oxidized by a proper oxidant, such as O$_2$ in air or dissolved oxygen in water, and thus, surface Ti^{3+} will be consumed rapidly [62]. These results demonstrate that the surface of brown TiO$_{2-x}$ is dominated by Ti^{4+}, excluding the presence of Ti^{3+}, indicating that a stoichiometric TiO$_2$ nanoshell was formed on the surfaces of nonstoichiometric Ti^{3+}-doped hollow nanocrystals. The thickness of the TiO$_2$ shell is greater than 5 nm, which is larger than the detection limit of XPS. Moreover, the brown coloration is stable in air for months without noticeable changes in the absorbance. However, the sample turns white after annealing in air at 600 °C for 5 h, which is caused by the diffusion of Ti^{3+} from the bulk to the surface, i.e., the dilution of the "color centers".

To demonstrate the existence of Ti^{3+} or oxygen vacancies on the nanocrystals, electron paramagnetic resonance (EPR) spectroscopy of the as-prepared and vacuum-activated samples under a low temperature of 100 K was conducted, and the results are shown in Fig. 9. The Ti^{3+}-doped hollow nanocrystals show highly intense signals at approximately g = 1.97–2.02. The signals observed at g = 1.9763 and g = 1.9913 are assigned to a paramagnetic Ti^{3+} center [63]. Recent studies have shown that various shapes of the Ti^{3+}-related ESR signals at g = 1.96–1.99 can be induced by H$_2$ treatments of anatase
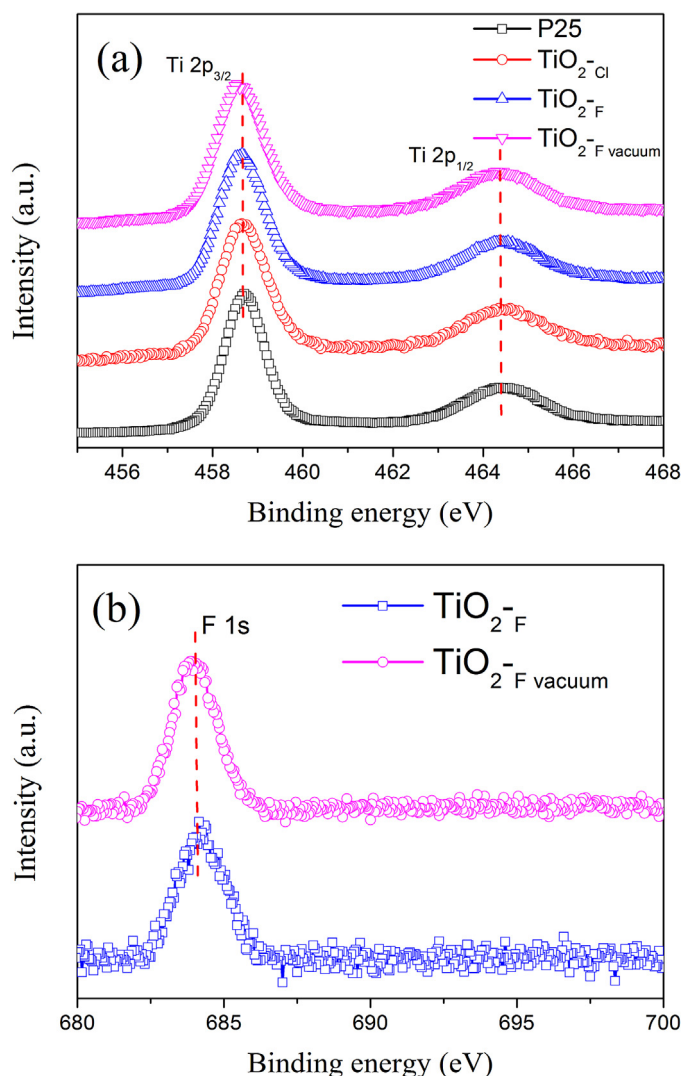
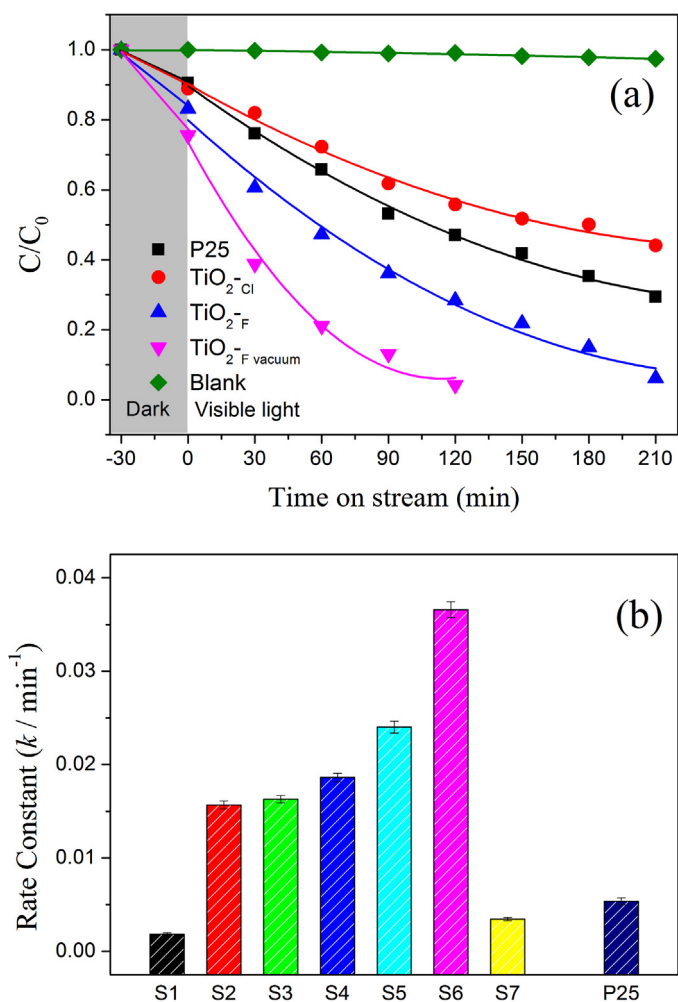**Fig. 8.** Fine XPS spectra of (a) Ti2p and (b) F1s of Degussa P25 and the TiO$_2$ obtained from [Bmim]Cl and [Bmim][BF$_4$] with and without vacuum treatment.
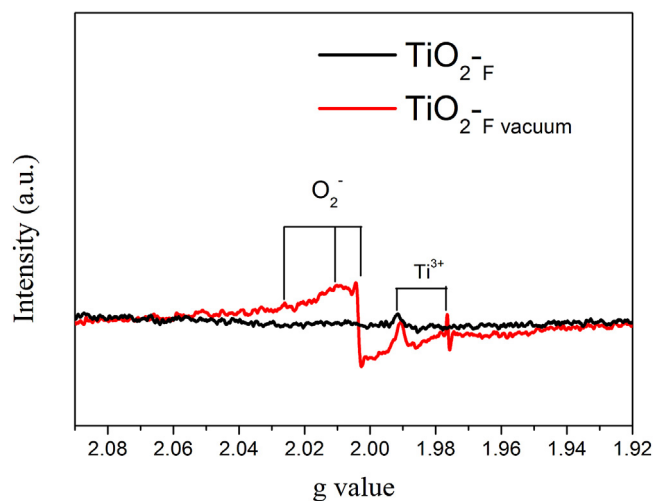
Fig. 9. EPR spectra of TiO$_2$ prepared from [Bmim][BF$_4$] with and without vacuum treatment.

Fig. 10. (a) Photodegradation of methylene blue (MB) under visible-light irradiation in the presence of various photocatalysts, and a blank experiment is provided as a control. (b) Comparison of the photocatalytic activity of P25 and TiO$_2$ samples prepared with varying Rf for the photocatalytic decolorization of MB aqueous solutions.

TiO$_2$ and F-doped TiO$_2$ [64,65]. The broad line signal at approximately g = 2.01, consisting of three sets of rhombic g values, could be assigned to superoxide species [66,67] (O^{2-}: g$_1$ = 2.002, g$_2$ = 2.009, and g$_3$ = 2.028). As reported in previous studies [29,54], during the vacuum activation, many O atoms departing from the TiO$_2$ lattices produce a large number of oxygen vacancies in TiO$_2$. Moreover, the electrons located in the oxygen vacancies can be transferred to the adjacent Ti^{4+} to generate the reduced Ti^{3+} centers. Thus, Ti^{3+} ions form in the nanocrystals, which is the cause for the bandgap shrinking and responsible for the strong visible absorption in the long wavelength range. This unique bandgap shrinking mechanism provides the Ti^{3+} self-doped TiO$_2$ with visible-light photocatalytic activity and superior stability, as demonstrated by the photodegradation of methylene blue (MB) and the selective oxidation of benzyl alcohol.

The photocatalytic activity of the Ti^{3+}-doped hollow nanocrystals was evaluated through the photodegradation of MB under visible light ($\lambda \geq 400$ nm) irradiation. A blank test revealed that the decoloration of MB was negligible within the test period in the absence of TiO$_2$. In the presence of anatase nanoparticles, however, decoloration occurred in each case, suggesting destruction of the absorption bands of MB. Fig. 10(a) shows a contradistinction in the photocatalytic degradation of MB on various TiO$_2$ photocatalysts. It is clearly observed that the vacuum-activated nanocrystals

synthesized from the ionic liquid [Bmim][BF$_4$] exhibit the highest performance. After irradiation for 90 min, approximately 97.3% of MB is photodegraded on the Ti^{3+}-doped hollow nanocrystals. In contrast, only 46.8% of MB is photodegraded on TiO$_2$ (P25). The inferior performances may largely be due to the Ti^{3+} incorporated into the TiO$_2$ lattice, which narrow the energy band gap of TiO$_2$ via forming intermediate energy levels, leading to a visible-light photocatalyst. Moreover, the larger surface areas and the wormhole structures were also expected to be able to provide more active sites and shorten the bulk diffusion length of charge carriers, thus suppressing bulk recombination. To quantitatively compare the photocatalytic performances of as-obtained TiO$_2$, the photocatalytic reactions were analyzed using the Langmuir-Hinshelwood pseudo-first-order kinetics model, and the reaction kinetics constant (k) is illustrated in Fig. 10(b). The results indicated that the molar ratio of the ionic liquid [Bmim][BF$_4$] in the solvothermal reaction system is an important factor that affects the photocatalytic activity of Ti^{3+} self-doped TiO$_{2-x}$. On the one hand, all of the samples prepared from [Bmim][BF$_4$] exhibited relatively higher photodegradation activity compared with that of the fluorine-free sample (S1). On the other hand, for the different fluorinated samples, the photodegradation activity first increased with increasing [Bmim][BF$_4$] content, reached a maximum at Rf = 2 and then began to decrease. However, when Rf was greater than 2, the photocatalytic activity rapidly decreased. The previous results indicate that high fluorine concentrations are not suitable for the fabrication of highly photoactive TiO$_2$ because F$^-$ can serve not only as a mediator of interfacial charge transfer but also as a recombination center [43].

To further test the oxidation activity of the Ti^{3+}-doped TiO$_2$ hollow nanocrystals, we employed the selective oxidation of benzyl alcohol at room temperature and ambient pressure as a probe reaction. Blank experiments (without photocatalyst) revealed negligible photocatalytic activities, verifying that the selective oxidation reaction is truly driven by a photocatalytic process. During the oxidation reactions, only benzaldehyde was detected under the experimental conditions, and the selectivity was greater than 99%. As shown in Fig. 11, all of these samples are visible-light-active for the photocatalytic selective oxidation of benzyl alcohol into benzaldehyde. Among all of the samples, the Ti^{3+}-doped hollow nanocrystals (S6) show the best visible-light photoactivity toward the selective oxidation of benzyl alcohol, which is almost 4.6 times higher than that of P25. A high photocatalytic activity of reduced TiO$_{2-x}$ under visible light illumination was observed, as previously reported by Hamdy et al. [68]. Although their blue titania catalysts exhibited better photoactivity and higher ketone selectivity than the commercial titania catalysts, they could not maintain such activity for a long period of time and were largely deactivated after the first run. Unlike previous experiments, our Ti^{3+}-doped hollow nanocrystals exhibited good recycling ability in the photocatalytic oxidation of benzyl alcohol and decoloration of MB (results shown in Fig. 12). This is due to the unique crystalline structure of the brown TiO$_{2-x}$ nanoparticle, which is composed of a defective and disordered core (TiO$_{2-x}$) and an intact shell (TiO$_2$). The stoichiometric TiO$_2$ shell effectively blocks oxidation between the Ti^{3+} and dissolved oxygen in water, thereby allowing long-term usage. Therefore, it is not surprising that our Ti^{3+} self-doped hollow nanocrystals for the selective oxidation of benzyl alcohol and degradation of MB still show very high photocatalytic activity after 5 cycles without an obvious decrease in activity.

Previous studies have proven that molecular oxygen is the oxidizing agent for many photo-oxidation processes that are catalyzed by TiO$_2$ [69,70]. Moreover, this process is dominated by the adsorption of molecular oxygen on the surface of TiO$_2$ during the photocatalytic reaction [71]. To better understand this process, we used different radical scavengers in controlled experiments to
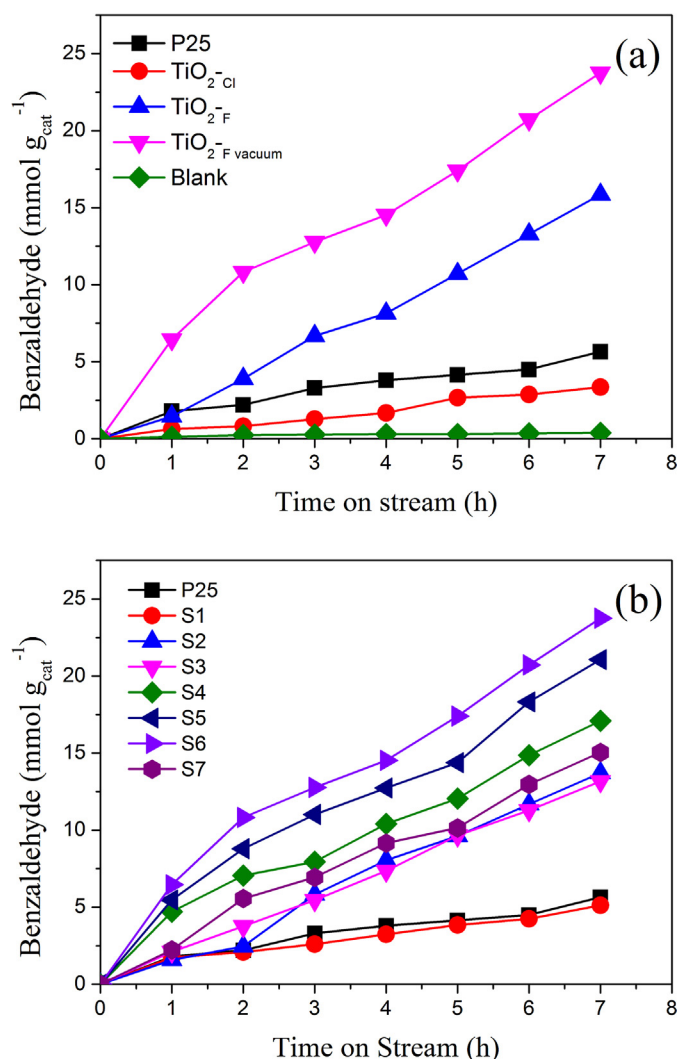
Fig. 11. (a) The photocatalytic oxidation of benzyl alcohol under visible-light irradiation in the presence of various photocatalysts, and a blank experiment is provided as a control. (b) Comparison of the photocatalytic activity of P25 and TiO_2 samples prepared with varying Rf for the photocatalytic selective oxidation of benzyl alcohol.
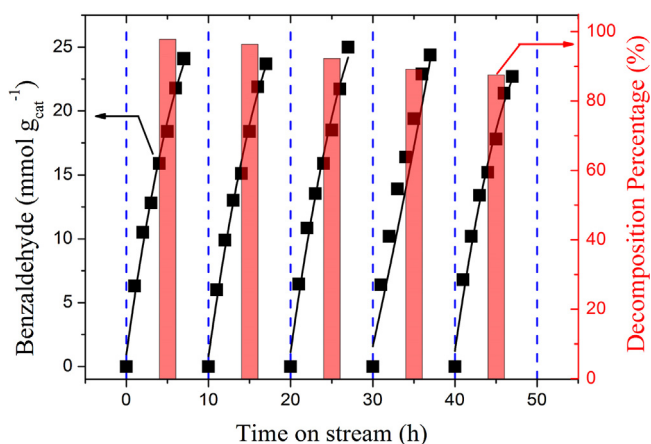
Fig. 12. Cycling runs in the photodegradation of MB and photooxidation of benzyl alcohol in the presence of Ti^{3+} self-doped TiO_2 hollow nanocrystals.
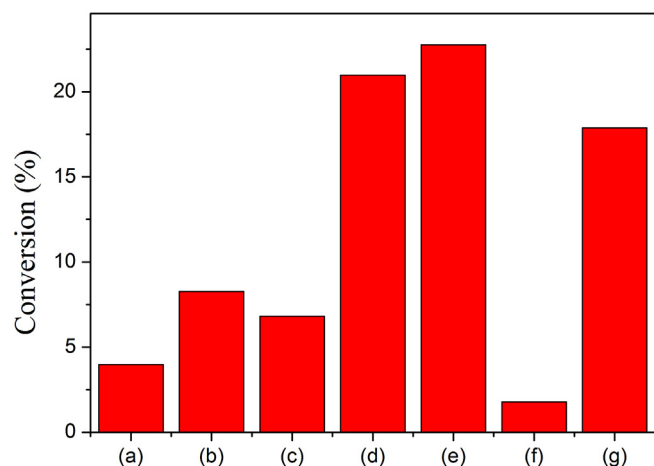
Fig. 13. Control experiments using different radical scavengers (a) $AgNO_3$ for photogenerated electrons, (b) *p*-benzoquinone (BQ) for superoxide radicals, (c) EDTA-2Na for photogenerated holes, (d) *tert*-butyl alcohol (TBA) for hydroxyl radicals, and (e) absence of radical scavengers for the photocatalytic selective oxidation of benzyl alcohol over Ti^{3+} self-doped TiO_2 hollow nanocrystals. Reaction under a nitrogen atmosphere (f) and air atmosphere (g).

probe the reaction mechanism for the selective oxidation of benzyl alcohol over Ti^{3+} self-doped TiO_2 hollow nanocrystals under visible-light irradiation. As shown in Fig. 13, no significant change in the reaction process was observed when TBA was added to the reaction system to capture •OH radicals [72]. However, an abrupt decrease in the conversion was observed upon the addition of either EDTA-2Na to capture photogenerated holes (h^+)[37], $AgNO_3$ to capture photoelectrons ($e-$) [73], or benzoquinone to capture •O^{2-} radicals [74]. Moreover, to investigate the role of molecular oxygen, the experiment was also conducted under nitrogen and air atmospheres. The trace conversion of benzyl alcohol in the nitrogen atmosphere was 1.8%, but in the air atmosphere, a higher conversion was obtained (17.9%), but this conversion was still less than that in pure oxygen (22.7%). These results demonstrated that molecular oxygen was the oxidant in the photooxidation process [75]. The reaction mechanism is thus briefly described in Fig. 14. By illuminating the catalyst with visible light, the electron is excited to the impurity level. Meanwhile, the molecular oxygen adsorbs at defect sites where electron density is available to form bonds between the surface and O_2, simultaneously producing superoxide radical groups. These superoxide species evolve into an alkoxide intermediate by cleaving the O—H bond of the alcohol. Then, the alkoxide intermediate can combine with a proton from the dehydrogenated species to produce H_2O_2, yielding benzaldehyde as the product. However, note that the conversion of benzyl alcohol is only 22.7%, compared to that of the latest research studies [76–81], which is still too low for photocatalytic applications. This is due to the low number of O_2 adsorption sites on the TiO_2 surface, and a large number of excited electrons are present in TiO_2 that can recombine with holes, thus limiting the photocatalytic activity of TiO_2. According to Musgrave's study [82], Pt clusters deposited on TiO_2 will provide electron density, and hence O_2 adsorption sites, that in effect allows more O_2 to interact with the TiO_2 surface. Furthermore, literature surveys [72,83] propose using a redox reaction between the reductive TiO_2 with oxygen vacancies and metal salt precursors, noble-metal nanoparticles (Ag, Pt, and Pd) are uniformly deposited on the defective TiO_{2-x} surface in the absence of any reducing agents or stabilizing ligands. Thus, further work is required to develop a new strategy for preparing defective semiconductor-based nanomaterials for target applications in solar energy conversion.
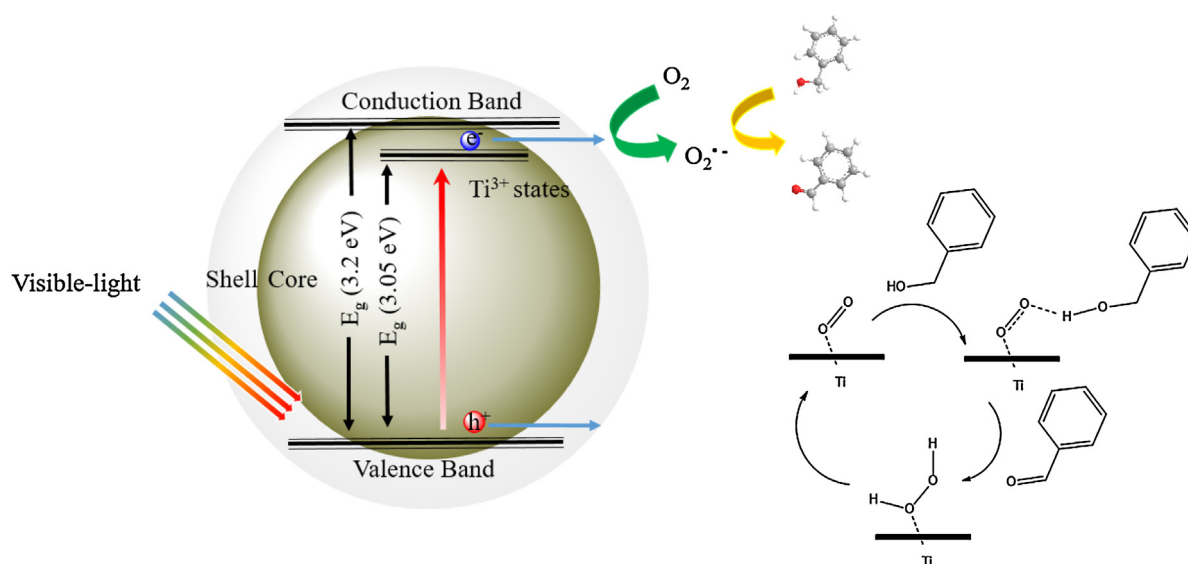
Fig. 14. Proposed mechanism for the selective oxidation benzyl alcohol under visible-light irradiation.

4. Conclusion

In summary, Ti^{3+} doped TiO_2 nanocrystals with a hollow structure were prepared via a microwave-assisted ionic liquid solvothermal approach, followed by a vacuum-activation method. The predominant advantages of this method are that it is fast, simple and relatively green. Moreover, the synthesized samples have been demonstrated to be highly photocatalytically active toward the selective oxidation of benzyl alcohol and the photodegradation of MB under visible light irradiation ($\lambda \geq 400$ nm). The highest photocatalytic activity is found for the sample prepared at the molar ratio of Rf = 2, which is more active than either P25 or other reduced TiO_{2-x} synthesized under the same conditions. Based on TEM, STEM, UV-DRS, PL, XPS, EPR, and Raman spectra analyses, it was found that the ionic liquid [Bmim][BF$_4$] plays a unique and critical role in obtaining TiO_2 nanocrystals and leading to wormhole structures, which are expected to be favorable for the diffusion and adsorption of reactant molecules, shorten the bulk diffusion length of charge carriers, and inhibit the photoelectron–hole recombination. Furthermore, the subsequent vacuum-activation process incorporates Ti^{3+} ions into the TiO_2 lattice, which narrow the energy band gap of TiO_2 via forming intermediate energy levels, thereby enhancing visible-light absorption. Moreover, the unique disordered core/ordered shell protects the TiO_{2-x} nanoparticle core from further oxidation and effectively blocks oxidation between the Ti^{3+} and dissolved oxygen in the solvent, thereby allowing long-term recycling stability. The present study demonstrates a simple and economical method for synthesizing Ti^{3+} self-doped TiO_2 with a hollow structure and develops a highly active photocatalyst under visible-light irradiation. It is hoped that our work can provide useful information and guide ongoing efforts for synthesizing defective semiconductor and defective semiconductor-based nanocomposite photocatalysts for solar energy conversion in heterogeneous photocatalysis.

Acknowledgements

Appendix A. Supplementary data

Supplementary data associated with this article can be found, in the online version, at http://dx.doi.org/10.1016/j.apcatb.2016.03.021.

References

[1] A. Fujishima, K. Honda, Nature 238 (1972) 37–38.
[2] R. Asahi, T. Morikawa, T. Ohwaki, K. Aoki, Y. Taga, Science 293 (2001) 269–271.
[3] H. Xu, S. Ouyang, L. Liu, P. Reunchan, N. Umezawa, J. Ye, J. Mater. Chem. A 2 (2014) 12642–12661.
[4] A.L. Linsebigler, G. Lu, J.T. Yates Jr., Chem. Rev. 95 (1995) 735–758.
[5] X. Chen, S.S. Mao, Chem. Rev. 107 (2007) 2891–2959.
[6] I.K. Konstantinou, T.A. Albanis, Appl. Catal. B Environ. 49 (2004) 1–14.
[7] Q. Xiang, J. Yu, M. Jaroniec, Chem. Soc. Rev. 41 (2012) 782–796.
[8] J.C. Yu, L. Zhang, Z. Zheng, J. Zhao, Chem. Mater. 15 (2003) 2280–2286.
[9] S.U.M. Khan, M. Al-Shahry, W.B. Ingler Jr., Science 297 (2002) 2243–2245.
[10] B. Liu, H.M. Chen, C. Liu, S.C. Andrews, C. Hahn, P. Yang, J. Am. Chem. Soc. 135 (2013) 9995–9998.
[11] L.G. Devi, R. Kavitha, Appl. Catal. B Environ. 140–141 (2013) 559–587.
[12] J. Li, K. Zhao, Y. Yu, L. Zhang, Adv. Funct. Mater. 25 (2015) 2189–2201.
[13] S. Hoang, S. Guo, N.T. Hahn, A.J. Bard, C.B. Mullins, Nano Lett. 12 (2012) 26–32.
[14] X. Chen, L. Liu, F. Huang, Chem. Soc. Rev. 44 (2015) 1861–1885.
[15] Z. Zhang, J.T. Yates Jr., in: J. Jupille, G. Thornton (Eds.), Defects at Oxide Surfaces, Springer International Publishing, Switzerland, 2015, pp. 81–121.
[16] J. Su, X. Zou, J.S. Chen, RSC Adv. 4 (2014) 13979–13988.
[17] X. Chen, L. Liu, P.Y. Yu, S.S. Mao, Science 331 (2011) 746–750.
[18] F. Zuo, K. Bozhilov, R.J. Dillon, L. Wang, P. Smith, X. Zhao, C. Bardeen, P. Feng, Angew. Chem. Int. Ed. 51 (2012) 6223–6226.
[19] L.R. Grabstanowicz, S. Gao, T. Li, R.M. Rickard, T. Rajh, D.J. Liu, T. Xu, Inorg. Chem. 52 (2013) 3884–3890.
[20] X. Xin, T. Xu, J. Yin, L. Wang, C. Wang, Appl. Catal. B Environ. 176–177 (2015) 354–362.
[21] X. Liu, S. Gao, H. Xu, Z. Lou, W. Wang, B. Huang, Y. Dai, Nanoscale 5 (2013) 1870–1875.
[22] Q. Zhu, Y. Peng, L. Lin, C.M. Fan, G.Q. Gao, R.X. Wang, A.W. Xu, J. Mater. Chem. A 2 (2014) 4429–4437.
[23] G. Li, Z. Lian, X. Li, Y. Xu, W. Wang, D. Zhang, F. Tian, H. Li, J. Mater. Chem. A 3 (2015) 3748–3756.
[24] K. Li, S. Gao, Q. Wang, H. Xu, Z. Wang, B. Huang, Y. Dai, J. Lu, ACS Appl. Mater. Interfaces 7 (2015) 9023–9030.
[25] M. Xing, W. Fang, M. Nasir, Y. Ma, J. Zhang, M. Anpo, J. Catal. 297 (2013) 236–243.
[26] B. Li, Z. Zhao, Q. Zhou, B. Meng, X. Meng, J. Qiu, Chem. Eur. J. 20 (2014) 14763–14770.
[27] Z. Wang, C. Yang, T. Lin, H. Yin, P. Chen, D. Wan, F. Xu, F. Huang, J. Lin, X. Xie, M. Jiang, Energy Environ. Sci. 6 (2013) 3007–3014.

[28] C. Yang, Z. Wang, T. Lin, H. Yin, X. Lü, D. Wan, T. Xu, C. Zheng, J. Lin, F. Huang, X. Xie, M. Jiang, J. Am. Chem. Soc. 135 (2013) 17831–17838.
[29] M. Xing, J. Zhang, F. Chen, B. Tian, Chem. Commun. 47 (2011) 4947–4949.
[30] S. Liu, W. Wang, J. Chen, J.G. Li, X. Li, X. Sun, Y. Dong, J. Mater. Chem. A 3 (2015) 17837–17848.
[31] W. Zhou, W. Li, J.Q. Wang, Y. Qu, Y. Yang, Y. Xie, K. Zhang, L. Wang, H. Fu, D. Zhao, J. Am. Chem. Soc. 136 (2014) 9280–9283.
[32] B. Qiu, M. Xing, J. Zhang, J. Am. Chem. Soc. 136 (2014) 5852–5855.
[33] Y. Yin, R.M. Rioux, C.K. Erdonmez, S. Hughes, G.A. Somorjai, A.P. Alivisatos, Science 304 (2004) 711–714.
[34] W. Jiao, L. Wang, G. Liu, G.Q. Lu, H.M. Cheng, ACS Catal. 2 (2012) 1854–1859.
[35] L. Ren, Y. Li, J. Hou, X. Zhao, C. Pan, ACS Appl. Mater. Interfaces 6 (2014) 1608–1615.
[36] X. Zhao, W. Jin, J. Cai, J. Ye, Z. Li, Y. Ma, J. Xie, L. Qi, Adv. Funct. Mater. 21 (2011) 3554–3563.
[37] F.T. Li, X.J. Wang, Y. Zhao, J.X. Liu, Y.J. Hao, R.H. Liu, D.S. Zhao, Appl. Catal. B Environ. 144 (2013) 442–453.
[38] D. Zhang, G. Li, X. Yang, J.C. Yu, Chem. Commun. 2009 (2009) 4381–4383.
[39] D. Zhang, G. Li, H. Wang, K.M. Chan, J.C. Yu, Cryst. Growth Des. 10 (2010) 1130–1137.
[40] T.R. Gordon, M. Cargnello, T. Paik, F. Mangolini, R.T. Weber, P. Fornasiero, C.B. Murray, J. Am. Chem. Soc. 134 (2012) 6751–6761.
[41] Q. Shi, Y. Li, E. Zhan, N. Ta, W. Shen, CrystEngComm 16 (2014) 3431–3437.
[42] Y. Zheng, J. Cai, K. Lv, J. Sun, H. Ye, M. Li, Appl. Catal. B Environ. 147 (2014) 789–795.
[43] K. Lv, Q. Xiang, J. Yu, Appl. Catal. B Environ. 104 (2011) 275–281.
[44] C. Li, P. Ma, P. Yang, Z. Xu, G. Li, D. Yang, C. Peng, J. Lin, CrystEngComm 13 (2011) 1003–1013.
[45] M. Baghbanzadeh, L. Carbone, P.D. Cozzoli, C.O. Kappe, Angew. Chem. Int. Ed. 50 (2011) 11312–11359.
[46] J. Yu, Q. Xiang, J. Ran, S. Mann, CrystEngComm 12 (2010) 872–879.
[47] A. Parker, M. Marszewski, M. Jaroniec, ACS Appl. Mater. Interfaces 5 (2013) 1948–1954.
[48] Y. Yang, G. Wang, Q. Deng, D.H.L. Ng, H. Zhao, ACS Appl. Mater. Interfaces 6 (2014) 3008–3015.
[49] V.K. Lamer, R.H. Dinegar, J. Am. Chem. Soc. 72 (1950) 4847–4854.
[50] K. Ding, Z. Miao, Z. Liu, Z. Zhang, B. Han, G. An, S. Miao, Y. Xie, J. Am. Chem. Soc. 129 (2007) 6362–6363.
[51] W. Zheng, X. Liu, Z. Yan, L. Zhu, ACS Nano 3 (2009) 115–122.
[52] K. Ding, Z. Miao, B. Hu, G. An, Z. Sun, B. Han, Z. Liu, Langmuir 26 (2010) 5129–5134.
[53] J. Yu, S. Liu, H. Yu, J. Catal. 249 (2007) 59–66.
[54] M. Xing, J. Zhang, B. Qiu, B. Tian, M. Anpo, M. Che, Small 11 (2015) 1920–1929.
[55] J. Yan, G. Wu, N. Guan, L. Li, Z. Li, X. Cao, Phys. Chem. Chem. Phys. 15 (2013) 10978–10988.
[56] G. Liu, H.G. Yang, X. Wang, L. Cheng, H. Lu, L. Wang, G.Q. Lu, H.M. Cheng, J. Phys. Chem. C 113 (2009) 21784–21788.
[57] J. Huo, Y. Hu, H. Jiang, C. Li, Nanoscale 6 (2014) 9078–9084.
[58] Q. Xiang, K. Lv, J. Yu, Appl. Catal. B Environ. 96 (2010) 557–564.
[59] H.G. Yang, C.H. Sun, S.Z. Qiao, J. Zou, G. Liu, S.C. Smith, H.M. Cheng, G.Q. Lu, Nature 453 (2008) 638–641.
[60] Y.W. Jun, M.F. Casula, J.H. Sim, S.Y. Kim, J. Cheon, A.P. Alivisatos, J. Am. Chem. Soc. 125 (2003) 15981–15985.
[61] B. Jiang, Y. Tang, Y. Qu, J.Q. Wang, Y. Xie, C. Tian, W. Zhou, H. Fu, Nanoscale 7 (2015) 5035–5045.
[62] W. Fang, M. Xing, J. Zhang, Appl. Catal. B Environ. 160–161 (2014) 240–246.
[63] X. Yu, B. Kim, Y.K. Kim, ACS Catal. 3 (2013) 2479–2486.
[64] D.G. Calatayud, T. Jardiel, M. Peiteado, F. Illas, E. Giamello, F.J. Palomares, D. Fernández-Hevia, A.C. Caballero, J. Phys. Chem. C 119 (2015) 21243–21250.
[65] F. Zuo, L. Wang, T. Wu, Z. Zhang, D. Borchardt, P. Feng, J. Am. Chem. Soc. 132 (2010) 11856–11857.
[66] S. Furukawa, T. Shishido, K. Teramura, T. Tanaka, ACS Catal. 2 (2012) 175–179.
[67] Q. Chen, W. Ma, C. Chen, H. Ji, J. Zhao, Chem. Eur. J. 18 (2012) 12584–12589.
[68] M.S. Hamdy, R. Amrollahi, G. Mul, ACS Catal. 2 (2012) 2641–2647.
[69] H. Kobayashi, S. Higashimoto, Appl. Catal. B Environ. 170–171 (2015) 135–143.
[70] S. Higashimoto, R. Shirai, Y. Osano, M. Azuma, H. Ohue, Y. Sakata, H. Kobayashi, J. Catal. 311 (2014) 137–143.
[71] S. Wendt, P.T. Sprunger, E. Lira, G.K.H. Madsen, Z. Li, J.Ø. Hansen, J. Matthiesen, A. Blekinge-Rasmussen, E. Lægsgaard, B. Hammer, F. Besenbacher, Science 320 (2008) 1755–1759.
[72] X. Pan, Y.J. Xu, J. Phys. Chem. C 117 (2013) 17996–18005.
[73] J. Wang, Z. Bian, J. Zhu, H. Li, J. Mater. Chem. A 1 (2013) 1296–1302.
[74] J. Kou, Z. Li, Y. Yuan, H. Zhang, Y. Wang, Z. Zou, Environ. Sci. Technol. 43 (2009) 2919–2924.
[75] X. Zhang, X. Ke, H. Zhu, Chem. Eur. J. 18 (2012) 8048–8056.
[76] D. Tsukamoto, Y. Shiraishi, Y. Sugano, S. Ichikawa, S. Tanaka, T. Hirai, J. Am. Chem. Soc. 134 (2012) 6309–6315.
[77] Y. Shiraishi, H. Sakamoto, Y. Sugano, S. Ichikawa, T. Hirai, ACS Nano 7 (2013) 9287–9297.
[78] Y. Sugano, Y. Shiraishi, D. Tsukamoto, S. Ichikawa, S. Tanaka, T. Hirai, Angew. Chem. Int. Ed. 52 (2013) 5295–5299.
[79] T. Jiang, C. Jia, L. Zhang, S. He, Y. Sang, H. Li, Y. Li, X. Xu, H. Liu, Nanoscale 7 (2015) 209–217.
[80] J. Wang, B. Li, T. Gu, T. Ming, J. Wang, P. Wang, J.C. Yu, ACS Nano 8 (2014) 8152–8162.
[81] S. Sarina, H. Zhu, E. Jaatinen, Q. Xiao, H. Liu, J. Jia, C. Chen, J. Zhao, J. Am. Chem. Soc. 135 (2013) 5793–5801.
[82] C.L. Muhich, Y. Zhou, A.M. Holder, A.W. Weimer, C.B. Musgrave, J. Phys. Chem. C 116 (2012) 10138–10149.
[83] Y. Xie, K. Ding, Z. Liu, R. Tao, Z. Sun, H. Zhang, G. An, J. Am. Chem. Soc. 131 (2009) 6648–6649.